Journal of Chromatography A, 1217 (2010) 1332–1342

Contents lists available at ScienceDirect

Journal of Chromatography A

journal homepage: www.elsevier.com/locate/chroma

Dispersion in retentive pillar array columns

Xiaohong Yan[a,b], Qiuwang Wang[a], Haim H. Bau[b,*]

[a] State Key Laboratory of Multiphase Flow in Power Engineering, Xi'an Jiaotong University, Xi'an, Shaanxi, 710049, China
[b] Department of Mechanical Engineering and Applied Mechanics, University of Pennsylvania, Philadelphia, PA 19104-6315, USA

ARTICLE INFO

Article history:
Received 23 October 2009
Received in revised form
14 December 2009
Accepted 21 December 2009
Available online 4 January 2010

Keywords:
Dispersion
Pillar array
Retention
Volume average
Plate height
Chromatography
Ordered column

ABSTRACT

The method of volume averaging is applied to estimate the Taylor–Aris dispersion tensor of solute advected in columns consisting of ordered pillar arrays with wall retention of the type used in chromatographic separation. The appropriate closure equations are derived and solved in a unit cell with periodic boundary conditions to obtain the dispersion tensor (or the reduced plate height) as a function of the Peclet number (reduced velocity); pillar pattern, shape and size; partition coefficient; and resistance to mass transfer. The contributions of the velocity profile, the wall adsorption, and the mass transfer resistance to the dispersion tensor are identified and delineated. The model is verified by comparing its predictions and obtaining favorable agreement with results of direct numerical simulations and with experimental data for columns containing ordered pillars. The model is then used to study the effect of pillars' shape and pattern on the longitudinal dispersion coefficient (plate height).

1. Introduction

Pressure-driven, liquid chromatography is a ubiquitous separation and purification technique. Most experimental investigations address band broadening in packed bed columns [1]. In recent years, with advances in microfabrication techniques, there has been a growing interest in columns comprised of ordered pillars. The use of ordered pillar arrays reduces variability from one column to another, improves data reproducibility, and reduces dispersion by providing uniform conditions along the flow path. Since microfabrication technology allows one to control the pillars' shapes and patterns, pillar-based columns are also amenable to optimization.

Below, we survey briefly the literature pertaining to separation and band broadening in columns comprising pillar arrays. Didierjean et al. [2] studied experimentally dispersion in non-retentive, ordered and disordered circular pillar arrays and observed that the flow patterns significantly affect the dispersion tensor. Various researchers [3,4,5] demonstrated experimentally that the longitudinal dispersion coefficients of ordered micropillar columns are significantly smaller than those of equivalent packed beds. Eghbali et al. [6] examined the contribution of the top and bottom surfaces to dispersion in nonporous pillar arrays. De Pra et al. [7] evaluated the permeability and separation performance of cylindrical and diamond-shaped pillars. De Malsche et al. [8,9] produced partly porous pillars and investigated dispersion under both nonretained and retained conditions, observing reduced plate heights (plate height/pillar diameter) as small as 0.9 even at relatively large retention factors. Recently, Illa et al. [10] obtained high performance, pressure-driven separation in ordered pillar arrays fabricated with an unmodified cyclo olefin polymer, which, due to its hydrophobicity, facilitated retention without a need for a separate stationary phase. All the works surveyed above were experimental in nature. Theoretical models are indispensable to guide designers of chromatographic columns and to improve understanding of columns' performances.

Given the great importance of dispersion in diverse disciplines, it is not surprising that there is a large body of theoretical works on estimating the dispersion tensor. Researchers have employed direct numerical simulations [11,12]; perturbation methods such as central-manifold [13,14] and multiscale expansions; moment-based methods [15–18]; and volume-averaging techniques [19–24]. Most of the theoretical studies focused on dispersion in porous columns without retention [16,17,20,21,23,24]. Just a few theoretical studies addressed retention in open columns [13,14,15,18] and hardly any in packed beds. In particular, Golay [14] examined the influence of a thin stationary phase on dispersion in open tubes with circular cross-sections and in two-dimensional conduits. Aris [15] considered concurrent flow of mobile and retentive (not necessarily thin) phases in open channels of various cross-sections. In his classical work, Giddings [13] accounted for

* Corresponding author. Tel.: +1 215 898 8363; fax: +1 215 573 6334.
E-mail address: bau@seas.upenn.edu (H.H. Bau).

0021-9673/$ – see front matter © 2009 Elsevier B.V. All rights reserved.
doi:10.1016/j.chroma.2009.12.069

various single-step reactions in the open chromatographic column to better understand the role of complex, multi-step processes. Dutta et al. [18] analyzed the dispersion in large aspect ratio microconduits of various cross-sections with thin retention layers and obtained an expression for the dispersion coefficient in the form previously suggested by Giddings [13]. Notably, Dutta et al. [18,25] pointed out that the longitudinal dispersion coefficient can be reduced by judiciously sculpting the conduit's cross-section. More-recently, Zhao and Bau [26] demonstrated that transverse circulation in the conduit's cross-section leads to a significant reduction in the longitudinal dispersion coefficient.

Brenner [16] extended Aris' method of moments to derive an expression for the dispersion tensor in a periodic porous medium (packed bed) without retention. With the aid of finite element simulations, Edwards et al. [17] used Brenner's model to calculate the longitudinal and lateral dispersion coefficients of two-dimensional flow in a spatially periodic array of circular cylinders. Carbonell and Whitaker [20] developed a volume-averaging theory to estimate the dispersion tensor in spatially periodic, porous media in the absence of retention. Eidsath et al. [21] confirmed Carbonell and Whitaker's theory by comparing their predictions with experimental data. Plumb and Whitaker [22] extended Carbonell and Whitaker's theory to account for porous particles that facilitate mass transport through their pores. Using the volume-averaging method, Amaral et al. [23] and Buyuktas and Wallender [24] calculated the dispersion tensor of two-dimensional ordered and disordered cylinder arrays without retention as a function of array pattern and the Reynolds number.

Gzil et al. [11] solved directly two-dimensional advection-diffusion equations accounting for retention to determine the plate height of pressure-driven chromatography in an ordered column consisting of cylindrical, porous pillars and demonstrated that columns comprised of ordered pillar arrays yield better separation than packed bed columns. In a subsequent paper, using direct numerical simulations, De Smet et al. [12] demonstrated that a conduit's bottom and top walls contribute significantly to band broadening. Although direct numerical simulations are a powerful tool to study the performance of chromatographic columns, their applicability is limited as three-dimensional simulations are time-consuming and can be applied for only relatively short columns.

In this study, we extend the volume-averaging theory of Carbonell and Whitaker [20] and derive a new expression for the dispersion tensor accounting for both retention and interfacial mass transfer (Section 2). We verify our theory by comparing its predictions with available theories for open columns (Section 3.1) and with our own direct numerical simulations (Section 3.2). Sections 4.1 and 4.2 compare our theoretical predictions with experimental data and with direct numerical simulations for columns comprised of pillar arrays. Sections 4.3 and 4.4 examine the effects of pillar pattern and geometry on the dispersion tensor. Section 4.5 analyzes our dispersion tensor in the framework of the ABC, Knox [27,28] equation. Section 5 concludes.

2. Volume-averaged equations

In this section, we extend Carbonell and Whitaker's [20] theory to derive the dispersion tensor in a periodic medium with retention. Fig. 1 depicts a representative unit cell of characteristic dimensions ℓ_x and ℓ_y consisting of a solid phase coated with a *thin* retention layer and a mobile phase. The theory requires the following assumptions:

(a) The characteristic dimensions of the column are much larger than the characteristic dimensions of the unit cell and the characteristic dimensions of the unit cell are much larger than those of the pore (micro) structure.
(b) The residence time of the mobile phase in the column is sufficiently long for the deviation of the concentration distribution from the average concentration to attain a quasi-steady state.
(c) The medium is homogeneous.

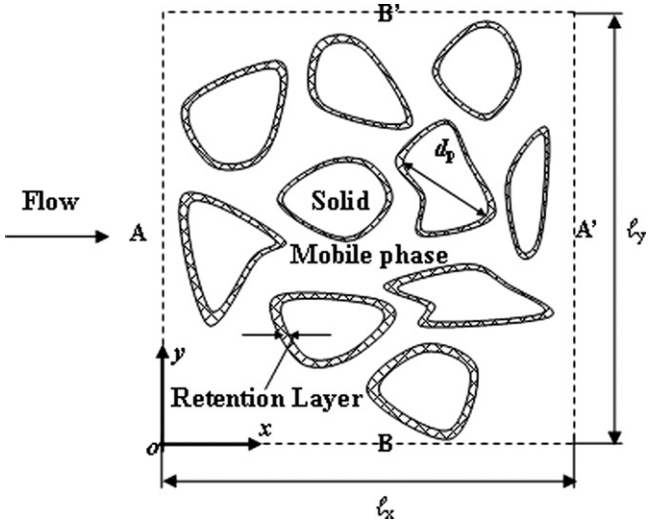

Fig. 1. Top view of a representative unit cell. The main flow is in the *x*-direction. The *z*-coordinate points out of the page.

Although our main focus is ordered pillar arrays, our theory is also applicable to random media.

The volume of the representative cell V is comprised of the volume of the mobile phase V_m, the volume of the stationary phase V_s where retention takes place, and the volume of the solid particle V_p.

$$V = V_m + V_s + V_p \tag{1}$$

In the above, we use, respectively, the subscripts m, s, and p to denote variables associated with the mobile, stationary, and solid phases.

We consider pressure-driven flow of incompressible solvent laden with analytes. The analytes are dilute, do not affect the solvent's properties, and do not interact. Consequently, we treat each analyte as if it existed all by itself. The fluid motion is described with the Navier–Stokes equation. The solvent obeys impermeability and nonslip boundary conditions at the interface between the mobile and stationary phases. There is no fluid flow in the stationary phase.

2.1. Volume averaging

The concentration of the analyte $C_m(\mathbf{r}, t)$ at position $\boldsymbol{r}$ and time t in a column of length L ($0 \le x \le L$) satisfies the advection-diffusion equation

$$\frac{\partial C_m}{\partial t} + \mathbf{v}\cdot\nabla C_m = D_m\nabla^2 C_m \quad (\text{in } V_m). \tag{2}$$

In the above, all quantities are dimensional. Bold letters represent vectors and light print letters represent scalars. The concentration of the analyte in the stationary phase $C_s(\mathbf{r}, t)$ satisfies the diffusion equation

$$\frac{\partial C_s}{\partial t} = D_s\nabla^2 C_s \quad (\text{in } V_s), \tag{3}$$

where D_m and D_s are, respectively, the uniform molecular diffusion coefficients of the analyte in the mobile and stationary phases. The

inlet concentration is $C_{in}\hat{\delta}(x)\hat{\delta}(t)$, where $\hat{\delta}(x)$ and $\hat{\delta}(t)$ are, respectively, the Dirac delta functions. The initial conditions are $C_m(\mathbf{r}, 0) = C_s(\mathbf{r}, 0) = 0$.

Mass conservation at the mobile phase-stationary phase interface (A_{ms}) requires continuity of fluxes [15]:

$$-D_s\mathbf{n}_{ms}\cdot\nabla C_s = -D_m\mathbf{n}_{ms}\cdot\nabla C_m = \delta\frac{\partial C_s}{\partial t} = k(\gamma C_m - C_s), \tag{4}$$

where $\mathbf{n}_{ms}$ is a unit vector normal to the interface directed away from the mobile phase; δ is the thickness of the stationary phase, which is assumed to be thin; and k and γ are, respectively, the mass transfer coefficient and the partition coefficient at the interface. When $k\to\infty$,

$$C_s = \gamma C_m \tag{5}$$

and the mobile and stationary phases are at local equilibrium at the mobile phase-stationary phase interface (A_{ms}). At the stationary phase-solid particle interface (A_{sp}),

$$D_s\mathbf{n}_{sp}\cdot\nabla C_s = 0. \tag{6}$$

To determine the velocity field, we solve the Navier–Stokes equations in a unit cell with periodic boundary conditions at the faces A–A′ and B–B′ (Fig. 1). To this end, the pressure in the axial direction is decomposed into a linearly decreasing component and a deviation from the linear behavior, i.e., $p(x, y, z) = -Bx + p'(x, y, z)$, where B plays the role of a body force.

Generally, due to the complex geometry, a direct numerical solution of Eqs. (2)–(6) is impractical. To estimate the dispersion tensor, we resort to volume averaging. We average Eqs. (2) and (3) over their respective domains and add up the resulting averaged equations.

$$\frac{\partial}{\partial t}\left(\langle C_m\rangle^m + \frac{V_s}{V_m}\langle C_s\rangle^s\right) + \nabla\cdot\langle\mathbf{v}C_m\rangle^m + \frac{1}{V_m}\int_{A_{ms}}\mathbf{n}_{ms}\cdot(\mathbf{v}C_m)dA = D_m\nabla\cdot\langle\nabla C_m\rangle^m + \frac{V_s}{V_m}D_s\nabla\cdot\langle\nabla C_s\rangle^s + \frac{1}{V_m}\int_{A_{ms}}D_m\mathbf{n}_{ms}\cdot\nabla C_m dA + \frac{V_s}{V_m}\cdot\frac{1}{V_s}\int_{A_{ms}}D_s\mathbf{n}_{sm}\cdot\nabla C_s dA \tag{7}$$

In the above, the symbol $\langle\,\rangle$ denotes an average over the domain specified in the superscript. For example, the volume-averaged concentration in the mobile phase ($\langle C_m\rangle^m$) and the area-average concentration at A_{ms} ($\langle C_m\rangle^{A_{ms}}$) are, respectively,

$$\langle C_m\rangle^m = \frac{1}{V_m}\int_{V_m} C_m\, dV \quad\text{and}\quad \langle C_m\rangle^{A_{ms}} = \frac{1}{A_{ms}}\int_{A_{ms}} C_m\, dA. \tag{8}$$

To obtain Eq. (7), we employed the spatial averaging theorem [20]

$$\langle\nabla\cdot\boldsymbol{\psi}\rangle = \nabla\cdot\langle\boldsymbol{\psi}\rangle + \frac{1}{V}\int_A\mathbf{n}\cdot\boldsymbol{\psi}\, dA \tag{9}$$

to transform the volume average of the derivative of any tensor $\boldsymbol{\psi}$ to a derivative of the averaged quantity. A is the surface area surrounding the volume V. Since there is no velocity component normal to the mobile–stationary phase interface, the area integral on the left hand side of Eq. (7) vanishes. Also, the last two terms on the right hand side of Eq. (7) cancel each other due to mass conservation (Eq. (4)). Finally, neglecting diffusion in the stationary phase, we reduce Eq. (7) to:

$$\frac{\partial}{\partial t}\left(\langle C_m\rangle^m + \frac{V_s}{V_m}\langle C_s\rangle^s\right) + \nabla\cdot\langle\mathbf{v}C_m\rangle^m = D_m\nabla\cdot\langle\nabla C_m\rangle^m. \tag{10}$$

Next, we define an average concentration for the entire unit cell

$$\langle C\rangle^{ms} = \frac{V_m\langle C_m\rangle^m + \gamma V_s\langle C_m\rangle^{A_{ms}}}{V_m + \gamma V_s} = \frac{\langle C_m\rangle^m + k''\langle C_m\rangle^{A_{ms}}}{1 + k''}, \tag{11}$$

where $V_m + \gamma V_s$ is the equivalent "mobile" volume and $k'' = \frac{\gamma V_s}{V_m}$ is the retention factor [12,27,28]. Next, we express the point concentration and velocity in terms of their average values and the deviations from the average:

$$C(\mathbf{r}, t) = \langle C(\mathbf{r}, t)\rangle^{ms} + C'(\mathbf{r}, t) \tag{12}$$

and

$$\mathbf{v}(\mathbf{r}, t) = \langle\mathbf{v}(\mathbf{r}, t)\rangle^m + \mathbf{v}'(\mathbf{r}, t). \tag{13}$$

Consistent with the Taylor–Aris dispersion theory, we assume that after a long time, $C'(\mathbf{r},t) \ll \langle C(\mathbf{r},t)\rangle^{ms}$. Consequently, the area-averaged concentrations equal approximately the volume-averaged concentrations, i.e., $\langle C_m\rangle^{A_{ms}} \approx \langle C_m\rangle^m$ and $\langle C_s\rangle^{A_{ms}} \approx \langle C_s\rangle^s$, and Eq. (11) yields $\langle C\rangle^{ms} = \langle C_m\rangle^m$. These approximations are discussed at length in Plumb and Whitaker [22] and will be verified later in the paper through comparisons with direct numerical simulations.

Accordingly, we re-write Eq. (10) as

$$\left(1 + k''\right)\frac{\partial\langle C\rangle^{ms}}{\partial t} + \langle\mathbf{v}\rangle^m\cdot\nabla\langle C\rangle^{ms} = D_m\nabla\cdot\left\{\nabla\langle C\rangle^{ms} + \frac{1}{V_m}\int_{A_{ms}}\mathbf{n}_{ms}C'\, dA\right\} - \nabla\cdot\langle\mathbf{v}'C'\rangle^m - \nabla\cdot\langle\langle\mathbf{v}\rangle^m C'\rangle^m - k''\frac{\partial\langle C_s/\gamma - C_m\rangle^{A_{ms}}}{\partial t}. \tag{14}$$

In the above, we set $\int_{A_{ms}}\boldsymbol{n}_{ms}\langle C\rangle^{ms}\, dA_{ms} \sim \langle C\rangle^{ms}\int_{A_{ms}}\boldsymbol{n}_{ms}\, dA_{ms} = 0$. The last term of Eq. (14) results from the departure from equilibrium at A_{ms}. This term decreases as k increases.

Next, we derive the equation for the deviation $C'(\boldsymbol{r}, t)$. To this end, we substitute Eq. (12) in Eq. (2) and subtract the volume-averaged concentration (Eq. (14)) to obtain

$$\mathbf{v}\cdot\nabla C' - D_m\nabla^2 C' - k''\frac{\partial\langle C\rangle^{ms}}{\partial t} + (\mathbf{v} - \langle\mathbf{v}\rangle^m)\cdot\nabla\langle C\rangle^{ms} = -\frac{\partial C'}{\partial t} - \nabla\cdot\left(\frac{1}{V_m}\int_{A_{ms}}D_m\mathbf{n}_{ms}C'\, dA\right) + \nabla\cdot\langle\mathbf{v}'C'\rangle^m + \nabla\cdot\langle\langle\mathbf{v}\rangle^m C'\rangle^m + k''\frac{\partial\langle C_s/\gamma - C_m\rangle^{A_{ms}}}{\partial t}. \tag{15}$$

According to the Taylor–Aris [15], Carbonell and Whitaker [20], and Plumb and Whitaker [22] theories, at long times, the first four terms on the RHS of Eq. (15) are all $O\left(\frac{\ell}{L}\right) << 1$. Since we consider conditions near equilibrium, we neglect the last term on the RHS of Eq. (15). Consequently, Eq. (15) reduces to

$$\mathbf{v}\cdot\nabla C' - D_m\nabla^2 C' = k''\frac{\partial\langle C\rangle^{ms}}{\partial t} - (\mathbf{v} - \langle\mathbf{v}\rangle^m)\cdot\nabla\langle C\rangle^{ms}. \tag{16}$$

Introducing the above approximation in Eq. (14) and neglecting diffusion, we obtain

$$k''\frac{\partial\langle C\rangle^{ms}}{\partial t} \approx -\frac{k''}{1 + k''}\langle\mathbf{v}\rangle^m\cdot\nabla\langle C\rangle^{ms}. \tag{17}$$

Substituting Eq. (17) in Eq. (16), we have

$$\mathbf{v}\cdot\nabla C' - D_m\nabla^2 C' = -\left(\mathbf{v} - \frac{\langle\mathbf{v}\rangle^m}{1 + k''}\right)\cdot\nabla\langle C\rangle^{ms}. \tag{18}$$

Next, we derive the boundary condition for $C'(\mathbf{r}, t)$. The flux at the mobile–stationary phases interface is:

$$J = -D_m\mathbf{n}_{ms}\cdot\nabla C_m = -D_m\mathbf{n}_{ms}\cdot\nabla\langle C\rangle^{ms} - D_m\mathbf{n}_{ms}\cdot\nabla C' \tag{19}$$

From Eq. (4)

$$J = \delta\frac{\partial C_s}{\partial t} = \gamma\delta\left(\frac{\partial C_m}{\partial t} + \frac{\partial(C_s/\gamma - C_m)}{\partial t}\right)$$

$$= \gamma\delta\left(\frac{\partial\langle C\rangle^{ms}}{\partial t} + \frac{\partial C'}{\partial t} + \frac{\partial(C_s/\gamma - C_m)}{\partial t}\right). \quad (20)$$

Since $C' \ll \langle C\rangle^{ms}$, and we assume near equilibrium conditions at the stationary phase–mobile phase interface. Eq. (20) reduces to

$$J = \gamma\delta\frac{\partial\langle C\rangle^{ms}}{\partial t}. \quad (21)$$

With the aid of Eq. (17), the boundary condition for C' becomes

$$D_m\mathbf{n}_{ms}\cdot\nabla C' = \left(-D_m\mathbf{n}_{ms} + \gamma\delta\frac{\langle\mathbf{v}\rangle^m}{1+k''}\right)\cdot\nabla\langle C\rangle^{ms}. \quad (22)$$

Finally, consistent with the definition of C', the volume average of C' in the volume $V_m + \gamma V_s$ is zero.

$$\int_{V_m} C'\,dV + \gamma\delta\int_{A_{ms}} C'\,dA = 0. \quad (23)$$

2.2. The closure problem

Eqs. (18), (22), and (23) constitute a linear boundary value problem for $C'(\boldsymbol{r}, t)$ with forcing (source) terms proportional to $\nabla\langle C\rangle^{ms}$. Accordingly, one seeks a solution of the form

$$C' = \mathbf{f}\cdot\nabla\langle C\rangle^{ms}, \quad (24)$$

where $\mathbf{f}(\boldsymbol{r})$ is a vector function of position in the unit cell. Substituting Eq. (24) in Eqs. (18), (22), and (23), we obtain the linear boundary value problem for $\mathbf{f}(\boldsymbol{r})$:

$$\mathbf{v}\cdot\nabla\mathbf{f} - D_m\nabla^2\mathbf{f} = -\left(\mathbf{v} - \frac{\langle\mathbf{v}\rangle^m}{1+k''}\right) \quad (25\text{-}1)$$

with the boundary condition

$$D_m\mathbf{n}\cdot\nabla\mathbf{f} = \left(-D_m\mathbf{n} + \gamma\delta\frac{\langle\mathbf{v}\rangle^m}{1+k''}\right), \quad (25\text{-}2)$$

at the mobile–stationary phase interface; the periodic boundary conditions

$$\mathbf{f}(x+\ell_x, y, z) = \mathbf{f}(x, y, z) \quad (25\text{-}3)$$

at the A–A′ interfaces and

$$\mathbf{f}(x, y+\ell_y, z) = \mathbf{f}(x, y, z) \quad (25\text{-}4)$$

at the B–B′ interfaces; and the normalization condition

$$\int_{V_m}\mathbf{f}\,dV + \gamma\delta\int_{A_{ms}}\mathbf{f}\,dA = 0. \quad (25\text{-}5)$$

Eqs. (25-1)–(25-4) allow us to determine $\mathbf{f}$ within an additive constant and Eq. (25-5) enforces uniqueness. Eqs. (25-1)–(25-5) can be solved numerically to obtain the vector function $\mathbf{f}$.

2.3. The dispersion tensor

Our objective is to transform Eq. (14) into a diffusion-advection-like equation. To this end, we start with the last term on the RHS of Eq. (14).

$$-k''\frac{\partial\langle C_s/\gamma - C_m\rangle^{A_{ms}}}{\partial t}$$

$$= -k''\frac{1}{k\gamma}\frac{\partial\left(\langle D_m\boldsymbol{n}_{ms}\cdot\nabla\langle C\rangle^{ms} + D_m\boldsymbol{n}_{ms}\cdot\nabla C'\rangle^{A_{ms}}\right)}{\partial t}$$

$$= -k''\frac{1}{k\gamma}\gamma\delta\frac{\langle\mathbf{v}\rangle^m}{1+k''}\cdot\frac{\partial\left(\nabla\langle C\rangle^{ms}\right)}{\partial t}$$

$$= -k''\frac{1}{k\gamma}\gamma\delta\frac{\langle\mathbf{v}\rangle^m}{1+k''}\cdot\nabla\left(\frac{\partial\langle C\rangle^{ms}}{\partial t}\right)$$

$$= \frac{(k'')^2}{(1+k'')^2}\frac{V_m}{k\gamma A_{ms}}\langle\mathbf{v}\rangle^m\langle\mathbf{v}\rangle^m : \nabla\nabla\langle C\rangle^{ms}. \quad (26)$$

In the above, the first transformation utilized Eq. (4); the second, Eq. (22); and the last, Eq. (17) and the spatial-invariance of the volume-averaged velocity. The second and third terms on the RHS of Eq. (14) can be written, respectively, as

$$-\nabla\cdot\langle\mathbf{v}'C'\rangle^m = -\langle v'\mathbf{f}\rangle^m : \nabla\nabla\langle C\rangle^{ms} \quad (27)$$

and

$$-\nabla\cdot\langle\langle\mathbf{v}\rangle^m C'\rangle^m = -\langle\langle\mathbf{v}\rangle^m\mathbf{f}\rangle^m : \nabla\nabla\langle C\rangle^{ms}$$

$$= \frac{\gamma\delta}{V_m}\langle\mathbf{v}\rangle^m\int_{A_{ms}}\mathbf{f}\,dA : \nabla\nabla\langle C\rangle^{ms}, \quad (28)$$

where the second transformation utilized Eq. (25-5).

Next, we re-write Eq. (14) in the form

$$(1+k'')\frac{\partial\langle C\rangle^{ms}}{\partial t} + \langle\mathbf{v}\rangle^m\cdot\nabla\langle C\rangle^{ms} = \boldsymbol{D} : \nabla\nabla\langle C\rangle^{ms}, \quad (29)$$

where the dispersion tensor

$$\boldsymbol{D} = D_m\left[\boldsymbol{I} + \frac{1}{V_m}\int_{A_{ms}}\boldsymbol{n}_{ms}\mathbf{f}\,dA\right] - \langle\mathbf{v}'\mathbf{f}\rangle^m$$

$$+ \frac{\gamma\delta}{V_m}\langle\mathbf{v}\rangle^m\int_{A_{ms}}\mathbf{f}\,dA + \frac{(k'')^2}{(1+k'')^2}\frac{V_m}{k\gamma A_{ms}}\langle\mathbf{v}\rangle^m\langle\mathbf{v}\rangle^m. \quad (30)$$

Using constraint Eq. (25-5), the dispersion tensor can be rewritten as

$$\boldsymbol{D} = D_m\left[\boldsymbol{I} + \frac{1}{V_m}\int_{A_{ms}}\boldsymbol{n}_{ms}\mathbf{f}\,dA\right] - \langle v\mathbf{f}\rangle^m + \frac{(k'')^2}{(1+k'')^2}\frac{V_m}{k\gamma A_{ms}}\langle\mathbf{v}\rangle^m\langle\mathbf{v}\rangle^m. \quad (31)$$

Only the symmetric components of the dispersion tensor contribute to the transport process. We use D_{xx} and D_{yy} to denote, respectively, the longitudinal and lateral dispersion coefficients. The dispersion tensor (Eq. (30)) consists of five terms. The first term represents molecular diffusion; the second term represents the effect of the tortuosity of the array of pillars (this term is absent in open conduits); the third term is due to hydrodynamic dispersion; the fourth term represents the effect of retention; and the fifth term represents the effect of mass transfer resistance. In the absence of a retentive layer ($k'' = \gamma = 0$, $k\to\infty$), Eq. (30) reduces to the well-known result $\boldsymbol{D} = D_m\left[\boldsymbol{I} + \frac{1}{V_m}\int_{A_{ms}}\boldsymbol{n}_{ms}\mathbf{f}\,dA\right] - \langle\mathbf{v}'\mathbf{f}\rangle^m$ [16,20,23,24]. When the velocity is uniform, the hydrodynamic dispersion term disappears. When the column is open, Eq. (30) reduces to the expression given by Aris [15] for a thin, non-diffusive stationary phase.

2.4. Decomposition of the dispersion tensor into flow-field and retentive contributions

Eq. (30) represents the contributions of the non-uniform velocity profile and the retention to the dispersion. To gain a better appreciation of the effects of the velocity and retention on dispersion, following Dutta et al. [18], we decompose $\mathbf{f}$ into two components:

$$\mathbf{f} = \mathbf{f}_0 + \frac{k''}{1+k''}\mathbf{f}_1. \quad (32)$$

where $\mathbf{f}_0$ is the solution of the boundary value problem

$$\mathbf{v}\cdot\nabla\mathbf{f}_0 - D_m\nabla^2\mathbf{f}_0 = -(\mathbf{v}-\langle\mathbf{v}\rangle^m), \tag{33-1}$$

$$-D_m\boldsymbol{n}\cdot\nabla\mathbf{f}_0 = D_m\boldsymbol{n}, \tag{33-2}$$

$$\mathbf{f}_0(x+\ell_x,y,z) = \mathbf{f}_0(x,y,z), \tag{33-3}$$

$$\mathbf{f}_0(x,y+\ell_y,z) = \mathbf{f}_0(x,y,z), \tag{33-4}$$

and

$$\int_{V_m}\mathbf{f}_0\,dV = -\gamma\delta\int_{A_{ms}}\mathbf{f}_0\,dA. \tag{33-5}$$

$\mathbf{f}_1$ is the solution of the boundary value problem

$$\mathbf{v}\cdot\nabla\mathbf{f}_1 - D_m\nabla^2\mathbf{f}_1 = -\langle\mathbf{v}\rangle^m, \tag{34-1}$$

$$-D_m\boldsymbol{n}\cdot\nabla\mathbf{f}_1 = -\frac{V_m}{A_{ms}}\langle\mathbf{v}\rangle^m, \tag{34-2}$$

$$\mathbf{f}_1(x+\ell_x,y,z) = \mathbf{f}_1(x,y,z), \tag{34-3}$$

$$\mathbf{f}_1(x,y+\ell_y,z) = \mathbf{f}_1(x,y,z), \tag{34-4}$$

and

$$\int_{V_m}\mathbf{f}_1\,dV = -\gamma\delta\int_{A_{ms}}\mathbf{f}_1\,dA. \tag{34-5}$$

We will see shortly that the normalization conditions (33-5) and (34-5) can be relaxed since the dispersion tensor will be recast into a form that is invariant to the transformation $\mathbf{f}\rightarrow\mathbf{f}+\mathbf{B}$, where $\mathbf{B}$ is any constant vector.

Similar to the treatment of dispersion in an open channel [18], we re-write the dispersion tensor (Eq. (30)) in the form:

$$\begin{aligned}\boldsymbol{D} = {} & D_m\boldsymbol{I} + D_m\left[\boldsymbol{g}_{\tau0} + \frac{k''}{1+k''}\boldsymbol{g}_{\tau1}\right] \\ & + \left[\boldsymbol{g}_{c0} + \frac{k''}{1+k''}\boldsymbol{g}_{c1} + \left(\frac{k''}{1+k''}\right)^2\boldsymbol{g}_{c2}\right] \\ & + \frac{(k'')^2}{(1+k'')^2}\frac{V_m}{k\gamma A_{ms}}\langle\mathbf{v}\rangle^m\langle\mathbf{v}\rangle^m,\end{aligned} \tag{35}$$

where

$$\boldsymbol{g}_{\tau0} = \frac{1}{V_m}\int_{A_{ms}}\boldsymbol{n}_{ms}\mathbf{f}_0\,dA, \tag{35-1}$$

$$\boldsymbol{g}_{\tau1} = \frac{1}{V_m}\int_{A_{ms}}\boldsymbol{n}_{ms}\mathbf{f}_1\,dA, \tag{35-2}$$

$$\boldsymbol{g}_{c0} = -\frac{1}{V_m}\int_{V_m}(\mathbf{v}-\langle\mathbf{v}\rangle^m)\mathbf{f}_0\,dV, \tag{35-3}$$

$$\begin{aligned}\boldsymbol{g}_{c1} = {} & -\frac{1}{V_m}\int_{V_m}(\mathbf{v}-\langle\mathbf{v}\rangle^m)\mathbf{f}_1\,dV + \langle\mathbf{v}\rangle^m \\ & \times\left(-\frac{1}{V_m}\int_{V_m}\mathbf{f}_0\,dV + \frac{1}{A_{ms}}\int_{A_{ms}}\mathbf{f}_0\,dA\right),\end{aligned} \tag{35-4}$$

and

$$\boldsymbol{g}_{c2} = \langle\mathbf{v}\rangle^m\left(-\frac{1}{V_m}\int_{V_m}\mathbf{f}_1\,dV + \frac{1}{A_{ms}}\int_{A_{ms}}\mathbf{f}_1\,dA\right). \tag{35-5}$$

Witness that when the vectors $\mathbf{f_i}$ are replaced with any constant vector, all the integrals that include $\mathbf{f_i}$ in the integrand vanish. Thus, expression (35) remains unchanged when one adds a constant vector to $\mathbf{f_i}$. This implies that the normalization conditions (33-5) and (34-5) are irrelevant. It is convenient to, respectively, replace equations (33-5) and (34-5) with equations such as $\langle\mathbf{f}_0\rangle^m = 0$ and $\langle\mathbf{f}_1\rangle^m = 0$. Another consequence of the above invariance is that the various tensors $\mathbf{g}_{ii}$ are independent of the retention process. Thus expression (35) allows us to assess how each process affects the dispersion tensor $\mathbf{D}$. The tensors $\boldsymbol{g}_{\tau0}$ and $\boldsymbol{g}_{\tau1}$ are associated with the medium's tortuosity. The tensor $\boldsymbol{g}_{c0}$ represents the contribution of the non-uniform velocity to the dispersion tensor. This contribution vanishes when the velocity profile is uniform. The terms $\boldsymbol{g}_{\tau1}$, $\boldsymbol{g}_{c1}$, and $\boldsymbol{g}_{c2}$ correspond to the retention's contribution to dispersion. In the presence of retention, the velocity field contributes to dispersion even when the velocity profile is uniform. The last term in Eq. (35) is due to the resistance to mass transfer.

2.5. Computational algorithm

Once we have defined the unit cell (i.e., Fig. 1), we solve the Navier–Stokes equations with periodic boundary conditions to obtain the flow-field. Then we solve Eqs. (25-1)–(25-5) to obtain the vector function $\mathbf{f}$. Once $\mathbf{f}$ has been determined, we compute the dispersion tensor with Eq. (31). All the computations were carried out with the multi-physics, finite element program Comsol™.

3. Model verification

To verify the theoretical model, we compared the theoretical predictions with prior theoretical and experimental works for open conduits and with direct numerical simulations of a pillar array.

3.1. Open column

Assuming uniform concentration in the stationary phase at any axial location and neglecting diffusion in the stationary phase, Golay [14] derived the expression

$$\frac{D_{xx}}{D_m} = 1 + Pe^2\left[\frac{1}{210} + \frac{1}{30}\frac{k''}{1+k''} + \frac{1}{12}\left(\frac{k''}{1+k''}\right)^2\right] \tag{36}$$

for longitudinal dispersion in flow between two parallel plates coated with thin retention layers. In the above, the Peclet number $Pe = \langle v_x\rangle^m d/D_m$ is based on the distance d between the parallel plates. Since in this case, the function $\mathbf{f}$ is one-dimensional, the closure problem (Eqs. (25-1)–(25-5)) can be solved in closed form to yield expression (36). To verify our numerical code, we defined a unit cell of length $\ell_x/d = 1$ and solved Eqs. (25-1)–(25-5) numerically to obtain a nearly perfect agreement (with less than 1% deviation) between our numerical results and Golay's theory (Eq. (36)).

3.2. Pillar array – comparison with direct numerical simulations (DNS)

Next, we solved directly the two-dimensional, time-independent momentum equation and the time-dependent advection-diffusion Eq. (2) with equilibrium boundary conditions at the surfaces of the retentive pillars (Eqs. (4) and (5)) and non-retentive boundary conditions at the conduit's surfaces. The computational domain consists of a conduit of length L and width W containing a single row of N (=120) pillars with pitch $\Lambda = W$ (Fig. 2a). The momentum equation was solved using periodic boundary conditions $p(x, y) = -Bx + p'(x, y)$, $p'(x+\Lambda, y) = p'(x, y)$, $\mathbf{v}(x+\Lambda, y) = \mathbf{v}(x, y)$, where B's magnitude was adjusted to yield the desired Peclet number. The concentration field satisfied the initial conditions

$$C(x,y,0) = \begin{cases}1 & 0 < x < \Lambda \\ 0 & \text{otherwise}\end{cases} \tag{37}$$

and the periodic condition

$$C(0,y,t) = C(L,y,t). \tag{38}$$

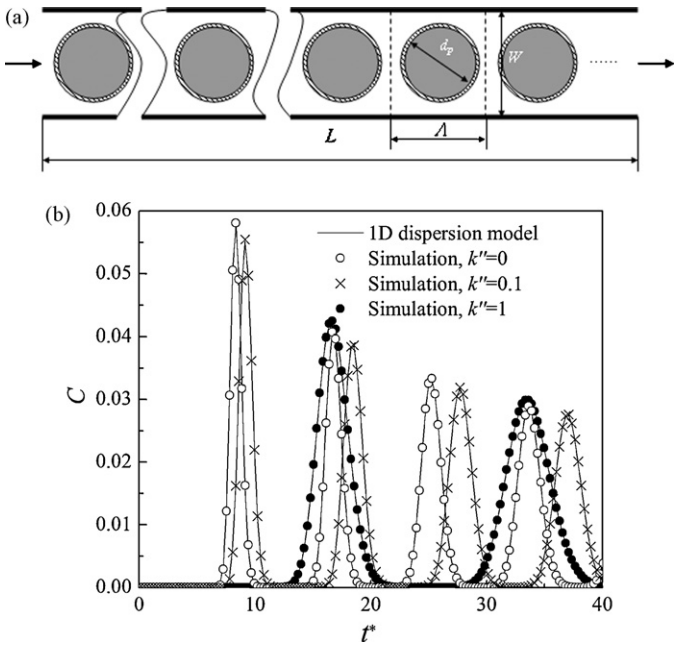

Fig. 2. (a) The computational domain. (b) The cross-section average concentration as a function of the dimensionless time t^* at nL when the retention factor $k''=0$ (hollow circular), 0.1 (×), and 1 (solid circles). The lines and symbols correspond, respectively, to the predictions of the one-dimensional, dispersion model and direct numerical simulations. $Pe=17.8$ and $k=\infty$.

Although the length of the computational domain is L, we obtain the concentration distribution in longer columns through the use of the periodic boundary conditions. The convergence of the computational results was verified through consecutive grid refinements.

To obtain the dispersion tensor (Eq. (30)), we calculated the vector function **f** (Eqs. (25-1)–(25-5)) in the unit cell framed with a dashed line in Fig. 2a. Fig. 2b depicts the cross-sectional average concentration $\langle C_{2D}(nL,t^*)\rangle = \frac{1}{W}\int_0^W C(nL,y,t^*)\,dy$ (symbols) calculated with the direct numerical simulation and the one-dimensional approximation $C_{1D}(nL,t^*)$ (solid line) calculated with the dispersion model as functions of the dimensionless time $t^* = \frac{D_m t}{d_p^2}$ when the retention factor $k''=0$, 0.1 and 1 and the Peclet number $Pe = \frac{\langle v_x\rangle^m d_p}{D_m} = 17.8$. Witness the excellent agreement between the predictions of the one-dimensional dispersion model and the direct numerical simulations. As the retention factor increased, the migration velocity of the solute band decreased. The velocity of the solute band's peak is $\langle v_x\rangle^m_{k''=0}/(1+k'')$, where $\langle v_x\rangle^m_{k''=0}$ is the peak's velocity in the absence of retention.

To determine the range of validity of the one-dimensional, dispersion model, Fig. 3 depicts the relative difference between the cross-section average concentrations predicted by the two-dimensional, direct numerical simulations and the one-dimensional model

$$\Delta C(X) = \frac{\int_0^\infty \left|\langle C_{2D}(X,t^*)\rangle - C_{1D}(X,t^*)\right|\ dt^*}{\int_0^\infty \langle C_{2D}(X,t^*)\rangle\, dt^*} \tag{39}$$

as a function of the dimensionless, axial position along the column. In the above, $X = \frac{xD_m}{\langle v_x\rangle^m d_p^2}$. The discrepancy between the one and two-dimensional models is smaller than 3% when $X>20$ (or $t^*>20$).

Next, we use the results of the 2D simulations to estimate the longitudinal dispersion coefficient (D_{xx}). To this end, we calculated

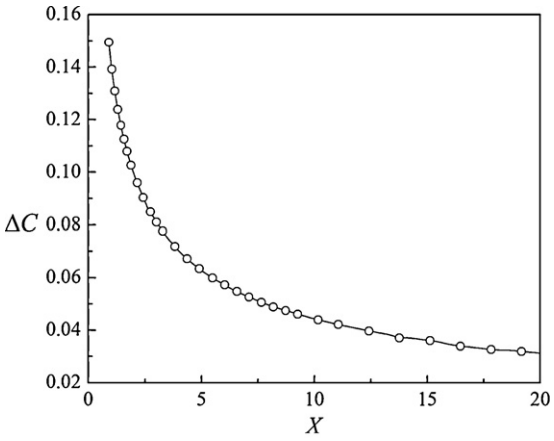

Fig. 3. The relative difference between the concentration peaks predicted with the two-dimensional, direct numerical simulations and the one-dimensional, dispersion model as a function of the dimensionless distance from the conduit's inlet. $Pe=17.8$, $k''=0$, and $k=\infty$.

the first moment

$$t_R(x) = \frac{\int_0^{t_\infty}\int_0^W tC(x,y,t)\ dydt}{\int_0^{t_\infty}\int_0^W C(x,y,t)\ dydt}, \tag{40-1}$$

and the variance

$$\sigma^2(x) = \frac{\int_0^{t_\infty}\int_0^W t^2C(x,y,t)\ dydt}{\int_0^{t_\infty}\int_0^W C(x,y,t)\ dydt} - t_R^2(x), \tag{40-2}$$

as functions of x. In the above, t_∞ is sufficiently large to allow the concentration to return to zero at position x. The longitudinal dispersion coefficient [11]

$$D_{xx}^{DNS}(x_j) = \frac{1}{2}\frac{\sigma^2(x_j)-\sigma^2(x_{j-1})}{t_R^2(x_j)-t_R^2(x_{j-1})}\langle v_x\rangle^m(x_j-x_{j-1}), \tag{40-3}$$

where x_j and x_{j-1} are two adjacent positions along the x-axis. Fig. 4 depicts the ratio between the dispersion coefficient estimated with Eq. (40-3) and the one (D_{xx}) calculated using the unit cell model (Eq. (30)) as a function of X. Consistent with other workers [1,18], we find that the volume-averaging technique provides excellent estimates of the longitudinal dispersion coefficient even at relatively small values of X. Our results are consistent with reports that in open conduits the longitudinal dispersion differs by less than 10% from its asymptotic value once $X>0.2$ [18].

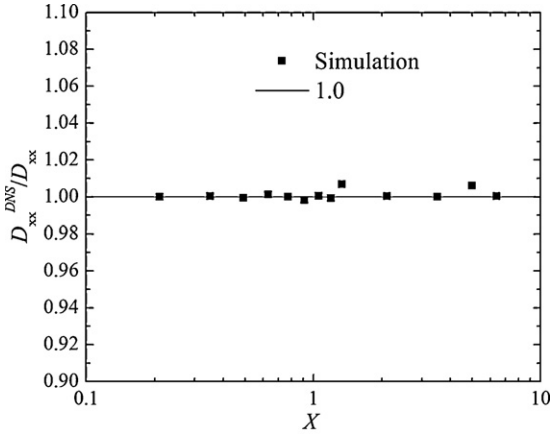

Fig. 4. The ratio of the dispersion coefficient estimated using direct numerical simulations and the dispersion coefficient predicted with the volume-averaging technique.

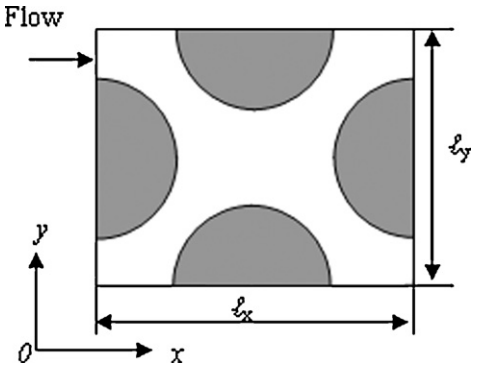

Fig. 5. A representative periodic, unit cell of the pillar array used in De Malsche et al.'s [8] experiments. The pillars are shown in gray. The geometry repeats itself both in the *x* and *y* directions.

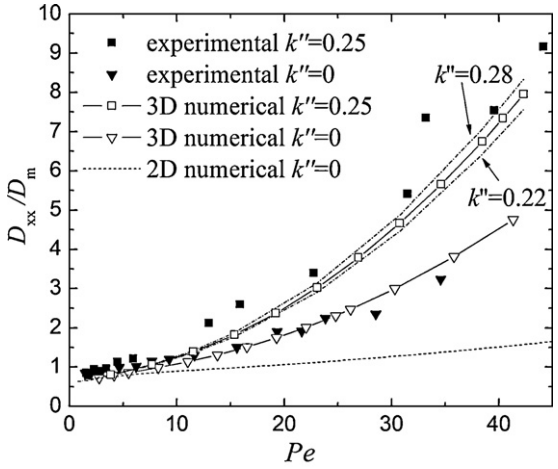

Fig. 6. The longitudinal dispersion coefficient normalized with the molecular diffusivity as a function of the Peclet number. The solid symbols correspond to experimental data [8]. The lines with hollow symbols correspond to our three-dimensional, theoretical predictions. The dotted line corresponds to our two-dimensional, theoretical predictions. $Sh = \infty$.

4. Results and discussion

4.1. Comparison between theoretical predictions and experimental data

De Malsche et al. [8] fabricated chromatographic columns consisting of 10 μm diameter, 19 μm tall pillars positioned at the vertexes of an equilateral, triangular grid. The conduit's width (W) was several hundreds of microns, and the pillars spanned the entire height of the conduit. Fig. 5 depicts a representative unit cell of the array's geometry ($\ell_x/\ell_y = \sqrt{3}$). The experimenters fabricated both smooth-surface pillars and pillars coated with a 550 nm thick porous layer (estimated porosity $\varepsilon_{int} = 0.73$). The external porosity (volume fraction of the mobile phase) is 0.4. In the experiments, the ratio of the average velocities of passive tracers too large to enter the pores ($\langle v_x \rangle^m_{k''=0}$) and passive tracers small enough to enter the pores ($\langle v_x \rangle^m_{k''=0}/(1+k'')$) was 1.25 ± 0.03. Accordingly, the retention factor of the porous layer is estimated as $k'' = 0.25$.

De Malsche et al. [8] measured band broadening of coumarin C480 suspended in methanol ($D_m = 8.6 \times 10^{-10}$ m^2/s). They observed that the side walls caused "bending" of the bands and reported only on the evolution of the portion of the band located close to the conduit's center, minimizing the effect of the side walls on the reported experimental data. As is common in chromatography, the experimenters summarized their data in terms of plate heights. To compare our theory with the experimental data, we converted the reported, reduced plate height (h) to the longitudinal dispersion coefficient using the formula $D_{xx}/D_m = h\,Pe/2$.

We computed the dispersion tensor using both 2D and 3D unit cells with periodic boundary conditions in both the *x* and *y* directions and neglected the effects of the side walls on dispersion as the latter was excluded from the experimental data. The three-dimensional computations accounted for the effects of the top and bottom surfaces on dispersion. Fig. 5 depicts the top view of the unit cell.

Fig. 6 compares our 2D (dashed line) and 3D (lines with hollow symbols) theoretical predictions with De Malsche et al.'s [8] experimental data (solid symbols). The figure depicts the longitudinal dispersion coefficient normalized with the molecular diffusivity as a function of the Peclet number. The squares and downright triangles correspond, respectively, to a column with an estimated retention factor of $k'' = 0.25$ (porous pillars) and a column without a stationary phase ($k'' = 0$, smooth pillars). We assume that the porous layer does not present resistance to mass transfer and $Sh \to \infty$. The Sherwood number $Sh = \frac{kd_p}{D_m}$. Witness the excellent agreement between the predictions of the three-dimensional theory and the experimental data both in the absence and the presence of a retentive layer. Not surprisingly, due to the effect of the top and bottom surfaces, the dispersion coefficient in the three-dimensional case is significantly larger than in the two-dimensional case. We will show later that the three-dimensional dispersion coefficient can be significantly reduced by appropriate sculpting of the pillar analogous to Dutta's proposal [18,25] for the open column with a rectangular cross-section. The dash-dot lines in the figure correspond to three-dimensional theoretical predictions with retention factor $k'' = 0.25 \pm 0.03$. The region between the two dash-dot lines corresponds to the uncertainty in the values of the retention factor as reported by De Malsche et al. [8].

In a second set of experiments, De Malsche et al. [5] used 4.3 μm diameter, 11.5 μm tall, smooth pillars, with a mobile phase volume fraction of 0.55 patterned in a 1 mm wide conduit. The distances between the pillars closest to the side walls and the side walls were adjusted to minimize side-wall induced dispersion. The pillars were covalently coated with a monolayer of hydrophobic C8-chains with a thickness of about 1% of a pillar's diameter. Experiments were carried out with the coumarin dyes C440, C460, and C480 suspended in methanol-water mixtures.

Fig. 7 depicts the experimentally measured (solid symbols), predicted with 3D simulations (lines with hollow symbols) and predicted with 2D simulations (dashed line) longitudinal dispersion

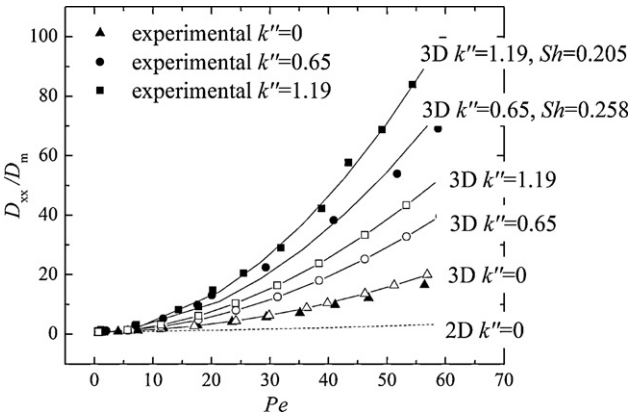

Fig. 7. The longitudinal dispersion coefficient normalized with the molecular diffusivity as a function of the Peclet number. The solid symbols correspond to experimental data [5]. The lines with hollow symbols correspond to our three-dimensional, theoretical predictions. The dotted line corresponds to two-dimensional, theoretical predictions.

coefficients as functions of the Peclet number. The upright triangles, circles, and squares correspond, respectively, to the cases with retention factors $k'' = 0$ (C440), 0.65 (C460), and 1.19 (C480) as reported in De Malsche et al. [5]. The band width was measured at the center of the conduit to exclude the effects of the side walls. Consistent with the experimental data, our computations did not account for the effects of the side walls. In the absence of retention ($k'' = 0$), the theoretical predictions are in excellent agreement with the experimental data. When $k'' > 0$ and $Sh = \infty$, the theory underpredicts (by about a factor of 1.8) the experimentally observed dispersion. We suspect that this discrepancy is caused because the simulations did not account for the resistance to mass transfer at the mobile phase-stationary phase interface. To check this hypothesis, we repeated the calculations including resistance to mass transfer. The mass transfer coefficient k was determined by solving an inverse problem in which we minimized the discrepancy between predictions and experimental data. We estimated $k = \infty$ ($Sh = \infty$), 7.2×10^{-5} m/s ($Sh = 0.26$), and 5.7×10^{-5} m/s ($Sh = 0.21$) for C440, C460, and C480, respectively. These values are consistent with experimentally measured mass transfer coefficients for C18-chains [29]. When we accounted for the resistance to mass transfer, the predictions were in excellent agreement with experimental observations. The calculations of Fig. 7 indicate that mass transfer resistance at the mobile phase–stationary phase interface plays a significant role in the longitudinal dispersion process.

4.2. Comparison of theoretical predictions with direct numerical simulations (DNS)

De Smet et al. [12] carried out 3D, direct numerical simulations with computational fluid dynamics software (FLUENT v.6.1) for both the nonporous, non-retentive pillar array and the porous, retentive pillar arrays. In the simulations, they specified pillar diameter $d_p = 5$ μm, and pillar heights $h_p = 5$, 10 and 12 μm. In all cases, the volume fraction of the mobile phase was 0.4. A sufficiently long computational domain was specified to allow one to reach nearly asymptotic plate height value. Fig. 8 depicts the normalized, longitudinal dispersion coefficient as a function of the Peclet number. The symbols correspond to De Smet et al.'s [12] direct numerical simulation data, and the lines correspond to our model's predictions. The model's predictions are in excellent agreement with the results of the direct numerical simulations.

4.3. The effect of array geometry on column performance

Since our model imposes minimal demands on computational resources, it can be conveniently used for parametric studies and

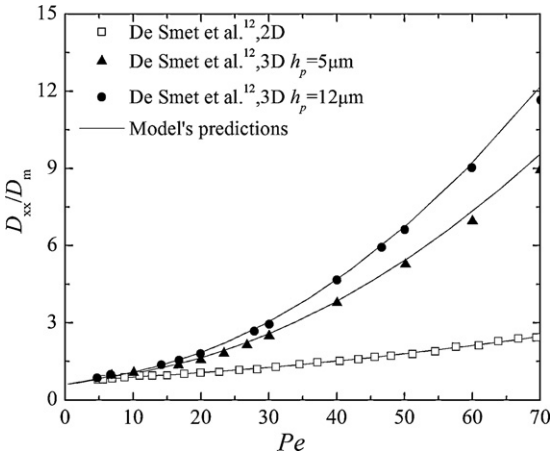

Fig. 8. The longitudinal dispersion coefficient (normalized with the molecular diffusivity) as a function of the Peclet number. The symbols correspond to De Smet et al.'s [12] direct numerical simulations. The lines correspond to our dispersion model's predictions. $k'' = 0$.

for optimization. For example, in chromatography, it is desirable to minimize the longitudinal dispersion coefficient and band broadening while in chemical reactors the opposite may be true. In this section, we examine briefly the effect of array pattern on the dispersion tensor.

We consider a two-dimensional pillar array with the pattern depicted in Fig. 5 (mobile phase volume fraction of 0.5). First, we examine the effect of the ratio ℓ_x/ℓ_y on the dispersion coefficient. Fig. 9a depicts the diagonal components of the dispersion tensor as functions of the Peclet number for several ℓ_x/ℓ_y ratios in the absence of retention ($k'' = 0$). As anticipated the dispersion coefficients increase as the Peclet number increases. The rate of increase, however, varies as a function of the aspect ratio ℓ_x/ℓ_y. In other words, the various curves intersect a few times. This indicates that the optimal geometry depends on the magnitude of the Peclet number. When $Pe > 100$, D_{xx} and D_{yy} are, respectively, proportional to Pe^a and Pe^b, where both a and b are functions of l_x/l_y, $1.7 < a < 2$ and $0.1 < b < 0.2$.

Fig. 9b depicts the normalized longitudinal and lateral dispersion coefficient as functions of the ratio ℓ_x/ℓ_y when $Pe = 10$, 50, and 100 and $k'' = 0$. The figure illustrates the existence of a minimum longitudinal (D_{xx}) dispersion coefficient. In the range of parameters considered here, the pattern ℓ_x/ℓ_y at which the minimum longitudinal dispersion coefficient occurs depends weakly on the Pe number. When $Pe < 100$, it appears reasonable to select $\ell_x/\ell_y \sim 1.4$. When

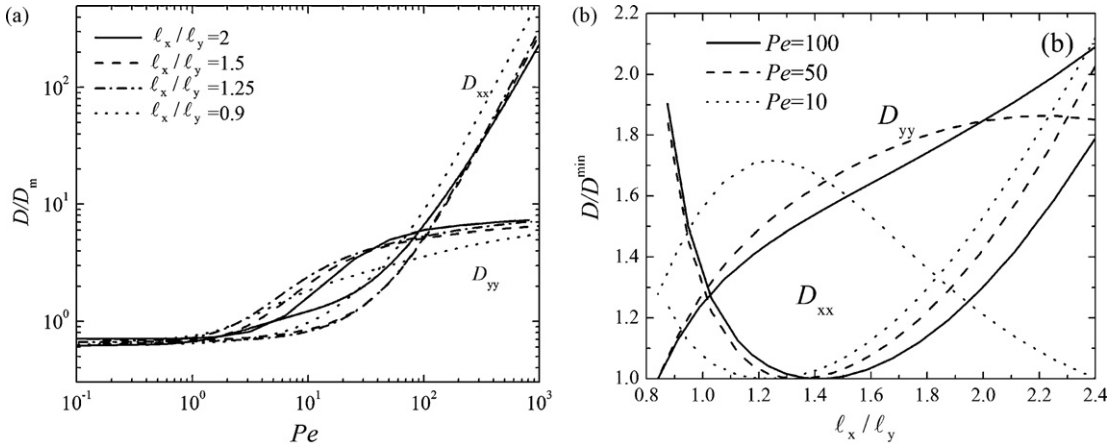

Fig. 9. The normalized longitudinal and lateral dispersion coefficients are depicted (a) as functions of the Peclet number for various ℓ_x/ℓ_y ratios and (b) as functions of ℓ_x/ℓ_y for various Peclet numbers. $k'' = 0$.

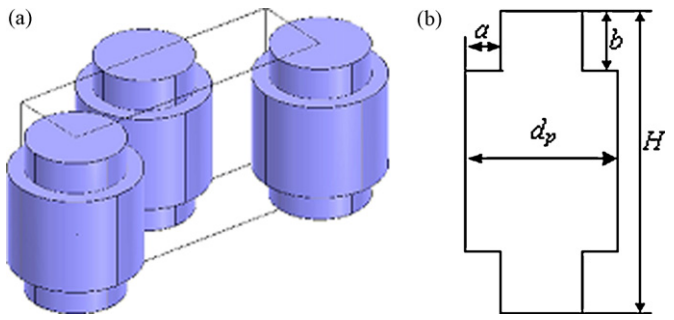

Fig. 10. (a) Three-dimensional image of pillars with undercuts. (b) The cross-section of a pillar with the undercuts.

the Peclet number is relatively small (i.e., $Pe = 10$), the ratio ℓ_x/ℓ_y that minimizes the longitudinal dispersion coefficient (D_{xx}) nearly coincides with the ratio ℓ_x/ℓ_y that maximizes the lateral dispersion coefficient (D_{yy}).

We have demonstrated in this section that by judicious selection of array pattern, it is possible to significantly reduce the longitudinal dispersion coefficient. Clearly, optimization of the pillars' shape and pattern is profitable.

4.4. Reducing the adverse impact of the top and bottom surfaces

Figs. 6–8 demonstrate a large difference between the longitudinal dispersion coefficients predicted by the two and three-dimensional models. This difference results from the presence of a floor and a ceiling in the 3D case, which retard the flow and significantly increase dispersion.

Dutta et al. [18,25] have showed that the longitudinal dispersion coefficient in open columns with nominally rectangular cross-sections can be significantly reduced by appropriate sculpting of the conduit's cross-section to increase the cross-sectional area available to the flow next to the side walls. Similar gains can be achieved with appropriate modifications of the pillars' geometry. Fig. 10 depicts the shape of a modified pillar with undercut (smaller diameter) regions next to the channel's floor and the ceiling to increase the flow velocity in these regions. We examine how the undercut affects the longitudinal dispersion coefficient while keeping the cross-sectional area available to the flow fixed. In other words, we keep $Hd_p - 4ab$ and the flow rate fixed while varying d_p, a, and b. Fig. 11 depicts the longitudinal dispersion coefficient as a function of the pillar's diameter–height ratio (d_p/H) with optimal undercuts (hollow circles and dashed line) and without (solid squares and solid line) undercuts. The dashed-dot line corresponds to the two-dimensional case (no floor and ceiling) and provides the lowest possible longitudinal dispersion coefficient at any given d_p/H. The Peclet numbers of the various cases considered in Fig. 11 varied slightly due to the variations in d_p. The figure illustrates that with appropriate modifications in the pillar's geometry, it is possible to reduce the longitudinal dispersion coefficient by as much as a factor of 5. Additional gains are likely with more rigorous optimization.

4.5. Implications for Knox ABC equation

Chromatographers often employ the Knox [28] ABC equation,

$$h = A \cdot Pe^n + B/Pe + C \cdot Pe, \tag{41}$$

to estimate the reduced (dimensionless) plate height (h) or the longitudinal dispersion coefficient $D_{xx} = (hD_m/2)Pe$, where $Pe = \langle v_x \rangle^m d_p/D_m$ is often referred to as the reduced velocity [27,28]. In Eq. (41), the plate height is normalized with the pillar diameter (d_p) in the case of a pillar array and with the bead diameter (d_p)

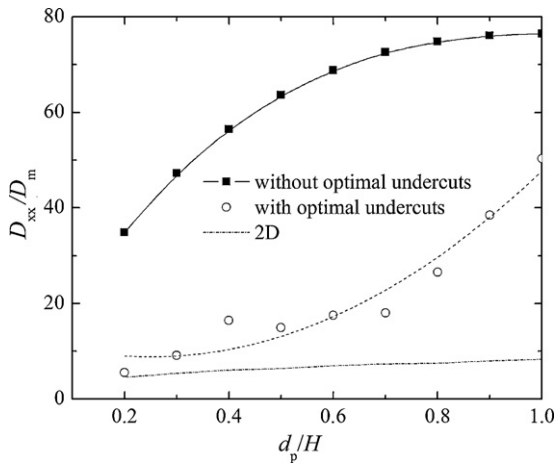

Fig. 11. The normalized, longitudinal dispersion coefficients of pillar arrays without (solid line) and with (dashed line) optimal undercuts as functions of the ratio between pillar diameter and height. The magnitude of the undercut was adjusted to preserve the cross-sectional area available to the flow. The horizontal, dashed-dot line corresponds to a two-dimensional case. $k'' = 0$.

in the case of a packed bed. Classically, the A, B, and C terms represent, respectively, the flow anisotropy; molecular, longitudinal diffusion; and mass transport; and they are determined empirically. In what follows, we will first determine the coefficients A, B, and C by fitting Eq. (41) with our dispersion theory's predictions and then we recast Eq. (35) in the form of the Knox equation.

4.5.1. Determination of A, B, and C by curve fitting

We determined A, B, and C by fitting Eq. (41) to our computed data (with $n = 1/3$). Fig. 12 depicts the normalized plate height of the various pillar arrays considered in the previous subsections as a function of the Peclet number in the absence ($k'' = 0$, hollow symbols) and presence ($k'' = 1$, solid symbols) of a retention layer. In all cases, the volume fraction of the mobile phase is 0.4. The upright triangles, squares, and circles correspond, respectively, to the staggered array [8] ($\ell_x/\ell_y = 1.73$, case I), the staggered array with an optimal pattern ($\ell_x/\ell_y = 1.4$, case II), and the staggered array with undercut pillars (Fig. 10, $\ell_x/\ell_y = 1.4$, case III). Solid lines are best fit curves generated with Eq. (41). Witness that Eq. (41) provides a

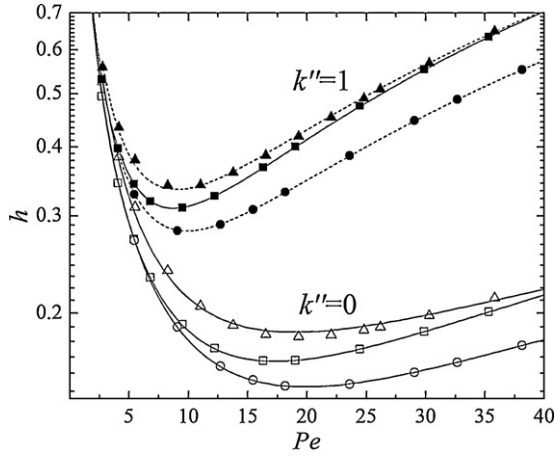

Fig. 12. The reduced plate height in the absence ($k'' = 0$, hollow symbols) and presence ($k'' = 1$, solid symbols) of a retention layer. The upright triangles, squares, and circles correspond, respectively, to the computational results for the staggered array ($\ell_x/\ell_y = 1.73$, case I, [8]), the staggered array with an optimal pillar pattern ($\ell_x/\ell_y = 1.4$, case II), and the staggered array with the undercut pillars (Fig. 10, $\ell_x/\ell_y = 1.4$, case III). The solid lines are best fit curves generated with Eq. (41). The porosity is 0.4, and the interfacial mass transfer coefficient $k \to \infty$.

Table 1
The values of the constants A, B, and C, the optimal Pe number, and the minimal plate height.

Retention	Geometry	A	B	C	Pe_{opt}	h_{min}
$k''=0$	$\ell_x/\ell_y=1.732$, case I	0.0232	1.3608	0.0027	19	0.185
	$\ell_x/\ell_y=1.4$, case II	0.0091	1.2819	0.0038	18	0.164
	$\ell_x/\ell_y=1.4$, case III	0.0083	1.3112	0.0030	20	0.147
$k''=1$	$\ell_x/\ell_y=1.732$, case I	0.0257	1.3498	0.0146	9.0	0.335
	$\ell_x/\ell_y=1.4$, case II	0.0127	1.2794	0.0157	8.6	0.301
	$\ell_x/\ell_y=1.4$, case III	0.0119	1.3090	0.0125	9.9	0.282

good fit to our theoretical data. The corresponding A, B, and C values for each case are documented in Table 1. Table 1 also lists the minimal, normalized plate height for each case and the Peclet number at which the minimum is attained.

The A value associated with the optimal geometry (case III) is significantly smaller than the other A values, which is consistent with the notion that A is mostly affected by processes taking place in the mobile phase. The A values in the absence of retention ($k''=0$) are, however, smaller than in the presence of retention ($k''=1$), indicating that A is not completely free of retention effects.

The C values in the absence of retention ($k''=0$) are significantly smaller than in the presence of retention ($k''=1$) and are not affected much by the pillar's pattern and geometry. The B values do not appear to vary much among the various cases.

4.5.2. Determination of A, B, and C by recasting the dispersion equation

Next, we attempt to recast Eq. (35) in the form of Eq. (41). We obtain the following expressions for A, B, and C.

$$A=\frac{2g_{c0}^{2D}}{D_m Pe^{n+1}},\quad B=2\left(1+g_{\tau 0}^{3D}+\frac{k''}{1+k''}g_{\tau 1}^{3D}\right),$$

$$C=C_{height}+C_{interface}+C_{stationary\text{-}diffusion}+C_{retention},$$

$$C_{height}=\frac{2(g_{c0}^{3D}-g_{c0}^{2D})}{D_m Pe^2},\quad C_{interface}=\left(\frac{k''}{1+k''}\right)^2\frac{2V_m D_m}{k\gamma A_{ms}d_p^2},$$

$$C_{stationary-diffusion}=0,$$

$$\text{and } C_{retention}=\frac{k''}{1+k''}\frac{2g_{c1}^{3D}}{D_m Pe^2}+\left(\frac{k''}{1+k''}\right)^2\frac{2g_{c2}^{3D}}{D_m Pe^2}. \quad (42)$$

In the above, g is the longitudinal component of the tensor $\mathbf{g}$ (Eqs. (35)) and the coefficients A, B, and C are, generally, functions of both the geometry and the Peclet number. The terms g_{c0}^{2D} and g_{c0}^{3D} denote, respectively, the values calculated for two-dimensional (without a floor and a ceiling) and three-dimensional pillar array columns. The terms C_{height}, $C_{interface}$, $C_{stationary\text{-}diffusion}$, and $C_{retention}$ represent, respectively, the contributions to the dispersion of the floor and ceiling, the mobile–stationary phase interfacial mass transfer resistance, the diffusion in the stationary phase, and the retention. In our work, the stationary phase is assumed to be thin, and the diffusion in the stationary phase is neglected: $C_{stationary\text{-}diffusion}\approx 0$. Various researchers have proposed different values of the exponent n [23,24].

We used Eq. (41) to calculate A, B, and C. Fig. 13 depicts A, B, and the various components of C as functions of the Peclet number for case **I** ($\ell_x/\ell_y=1.732$, $k''=1$, porosity 0.4, $k\to\infty$, and $n=1/3$). Similar trends were observed for cases II and III, but are not reproduced here in the interest of space. Since we do not consider diffusion in the stationary phase and $k\to\infty$, $C_{stationary\text{-}diffusion}=C_{interface}=0$. In the range of parameters considered In Fig. 13, B, C_{height}, and $C_{retention}$ are nearly independent of the Peclet number. In contrast, when $Pe<20$, A varies with the Pe number. Our data correlates reasonably well with an expression in the form $A\,Pe^n=A_0+A_1\,\ln(Pe)+A_2\,Pe$

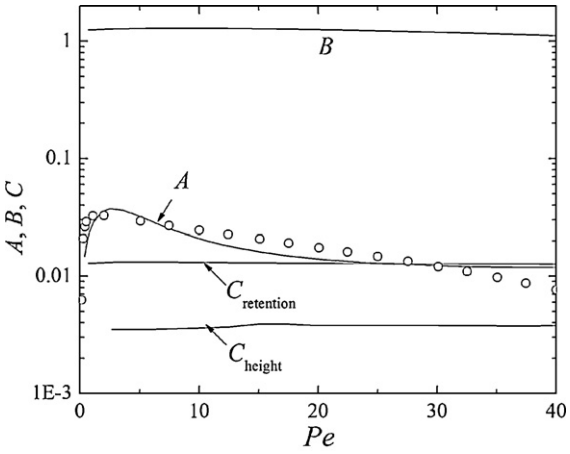

Fig. 13. The coefficients A, B, and C predicted by our dispersion theory for the staggered array ($\ell_x/\ell_y=1.73$, case I) are depicted as functions of the Peclet number. The hollow circles correspond to a logarithmic approximation for A. The porosity is 0.4, and the interfacial mass transfer coefficient $k\to\infty$.

[30] (hollow circles in Fig. 13). The averages of the A, B, and C values depicted in Fig. 13 are within 16% of the values reported in Table 1. In other words, if one were to use a Knox-like equation with the average values of A, B, and C based on Eq. (42), one would likely incur an error on the order of 14% when estimating the dispersion coefficient.

Various researchers have reported A values on the order of one for packed bed columns. Our theoretical estimates of A for columns comprised of ordered pillar arrays are much smaller in magnitude. This is consistent with Knox's argument that perfectly ordered, internal structures improve the column's performance. Since the A-term of the perfectly ordered column is small, the relative importance of the C term increases. See Figs. 7 and 12. Indeed, experimenters [9] reported relatively large C values in studies of columns consisting of ordered pillars coated with porous shells. Hence, stationary phases with small mass transfer resistance are critical for further optimization of the separation performance.

5. Conclusions

Using the volume-averaging technique, we derived a new formula to estimate the dispersion tensor in ordered pillar array columns with a thin retentive layer. The model accounts for both the retention and the resistance to mass transfer at the mobile–stationary phase interface. The model requires numerical computations over a domain consisting of a periodic unit cell. In contrast to direct numerical simulations, these computations do not heavily task computer resources and can be used for parametric and optimization studies. The dispersion tensor was decomposed into independent components identifying how geometry, velocity profile, retention, and resistance to mass transfer affect dispersion.

The model was verified by comparing its predictions with other models available in the literature, with results of direct numerical simulations, and with experimental data. In all cases, our model predictions were in good agreement with experimental data and with the results of direct numerical simulations.

Detailed results were presented for columns consisting of ordered pillar arrays. Such columns have advantages over columns comprised of packed beds. The ordered columns provide a uniform structure with a smaller longitudinal dispersion than in non-homogeneous structures. Moreover, the ordered columns assure consistency and reproducibility from one column to another,

reducing the variability of experimental data. Significantly, one can optimize the pattern of the array and the shape of the pillars to meet desired objectives. Although in this study we did not carry out rigorous optimization, we did demonstrate that by judicious selection of pillar pattern and shape one can reduce the longitudinal dispersion coefficient and minimize the adverse effects of the conduit's floor and ceiling. Obviously, much more can and should be done along these lines.

Finally, we discussed our results in the context of Knox's ABC equation, which is often used by chromatographers. We provided explicit expressions for the coefficients *A*, *B*, and *C*. Our results indicate that the value of *A* depends on the Peclet number while, for the cases studied here, *B* and *C* can be regarded as nearly independent of the Peclet number.

Acknowledgment

The work was supported, in part, by NSF STTR grant #0822723 to SFC Fluidics (HHB) and the China State Scholarship Fund (XY).

References

[1] N.W. Han, J. Bhakta, R.G. Carbonell, AIChE J. 31 (1985) 277.
[2] S. Didierjean, H.P. Amaral Souto, R. Delannay, C. Moyne, Chem. Eng. Sci. 52 (1997) 1861.
[3] M. De Pra, W.Th. Kok, J.G.E. Gardeniers, G. Desmet, S. Eeltink, J.W. van Nieuwekasteele, P.J. Schoenmakers, Anal. Chem. 78 (2006) 6519.
[4] H. Eghbali, W. De Malsche, D. Clicq, H. Gardeniers, G. Desmet, LCGC Eur. 4 (2007) 208.
[5] W. De Malsche, H. Eghbali, D. Clicq, J. Vangelooven, H. Gardeniers, G. Desmet, Anal. Chem. 79 (2007) 5915.
[6] H. Eghbali, W. De Malsche, J. De Smet, J. Billen, M. De Pra, W.T. Kok, P.J. Schoenmakers, H. Gardeniers, G. Desmet, J. Sep. Sci. 30 (2007) 2605.
[7] M. De Pra, W. De Malsche, G. Desmet, P.J. Schoenmakers, W.T. Kok, J. Sep. Sci. 30 (2007) 1453.
[8] W. De Malsche, D. Clicq, V. Verdould, P. Gzil, G. Desmet, H. Gardeniers, Lab Chip 7 (2007) 1705.
[9] W. De Malsche, H. Gardeniers, G. Desmet, Anal. Chem. 80 (2008) 5391.
[10] X. Illa, W. De Malsche, J. Bomer, H. Gardeniers, J. Eijkel, J.R. Morante, A.R. Rodriguez, G. Desmet, Lab Chip 9 (2009) 1511.
[11] P. Gzil, N. Vervoort, G.V. Baron, G. Desmet, Anal. Chem. 75 (2003) 6244.
[12] J. De Smet, P. Gzil, G.V. Baron, G. Desmet, J. Chromatogr. A 1154 (2007) 189.
[13] J.C. Giddings, J. Chromatogr. A 5 (1961) 46.
[14] M.J.E. Golay, in: D.H. Desty (Ed.), Gas Chromatography, Butterworth, Sci. Publ, London, 1958, p. 36.
[15] R. Aris, Proc. R. Soc. Lond. Ser. A 252 (1959) 538.
[16] H. Brenner, Phil. Trans. R. Soc. Lond. A297 (1980) 81.
[17] D.A. Edwards, M. Shapiro, H. Brenner, M. Shapira, Transport Porous Med. 6 (1991) 337.
[18] D. Dutta, D.T. Leighton, Anal. Chem. 75 (2003) 57.
[19] S. Whitaker, AIChE J. 13 (1967) 420.
[20] R.G. Carbonell, S. Whitaker, Chem. Eng. Sci. 38 (1983) 1795.
[21] A. Eidsath, R.G. Carbonell, S. Whitaker, L.R. Herrmann, Chem. Eng. Sci. 38 (1983) 1803.
[22] O.A. Plumb, S. Whitaker, in: J.H. Cushman (Ed.), Dynamics of Fluids in Hierarchical Porous Media, Academic Press, 1990.
[23] H.P. Amaral Souto, C. Moyne, Phys. Fluids 9 (1997) 2253.
[24] D. Buyuktas, W.W. Wallender, Heat Mass Transfer 40 (2004) 261.
[25] D. Dutta, A. Ramachandran, D.T. Leighton, Microfluid Nanofluid 2 (2006) 275.
[26] H. Zhao, H.H. Bau, Anal. Chem. 79 (2007) 7792.
[27] J.H. Knox, J. Chromatogr. A 831 (1999) 3.
[28] J.H. Knox, J. Chromatogr. A 960 (2002) 7.
[29] F. Gritti, G. Guiochon, J. Chromatogr. A 1216 (2009) 4752.
[30] D.L. Koch, J.F. Brady, J. Fluid Mech. 154 (1985) 399.